Pattern Recognition Letters 150 (2021) 8–16

Contents lists available at ScienceDirect

Pattern Recognition Letters

journal homepage: www.elsevier.com/locate/patrec

MIDCAN: A multiple input deep convolutional attention network for Covid-19 diagnosis based on chest CT and chest X-ray

Yu-Dong Zhang[a,1], Zheng Zhang[b,c,1], Xin Zhang[d,*], Shui-Hua Wang[e,*]

[a] School of Informatics, University of Leicester, Leicester, LE1 7RH, UK
[b] Shenzhen Key Laboratory of Visual Object Detection and Recognition, Harbin Institute of Technology, Shenzhen 518055, China
[c] Department of Computer and Information Science, University of Macau, Macau 999078, China
[d] Department of Medical Imaging, The Fourth People's Hospital of Huai'an, Huai'an, Jiangsu Province, 223002, China
[e] School of Mathematics and Actuarial Science, University of Leicester, LE1 7RH, UK

ARTICLE INFO

Article history:
Received 3 March 2021
Revised 14 May 2021
Accepted 23 June 2021
Available online 14 July 2021

Edited by: Maria De Marsico

Keywords:
Deep learning
Data harmonization
Multiple input
Convolutional neural network
Automatic differentiation
COVID-19
Chest CT
Chest X-ray
Multimodality

ABSTRACT

Background: COVID-19 has caused 3.34m deaths till 13/May/2021. It is now still causing confirmed cases and ongoing deaths every day.

Method: This study investigated whether fusing chest CT with chest X-ray can help improve the AI's diagnosis performance. Data harmonization is employed to make a homogeneous dataset. We create an end-to-end multiple-input deep convolutional attention network (MIDCAN) by using the convolutional block attention module (CBAM). One input of our model receives 3D chest CT image, and other input receives 2D X-ray image. Besides, multiple-way data augmentation is used to generate fake data on training set. Grad-CAM is used to give explainable heatmap.

Results: The proposed MIDCAN achieves a sensitivity of 98.10±1.88%, a specificity of 97.95±2.26%, and an accuracy of 98.02±1.35%.

Conclusion: Our MIDCAN method provides better results than 8 state-of-the-art approaches. We demonstrate the using multiple modalities can achieve better results than individual modality. Also, we demonstrate that CBAM can help improve the diagnosis performance.

1. Introduction

COVID-19 (also known as coronavirus) pandemic is an ongoing infectious disease caused by severe acute respiratory syndrome (SARS) coronavirus 2 [1]. As of 13/May/2021, there are over 161.14m confirmed cases and over 3.34m deaths attributed to COVID-19. The cumulative deaths of the top 10 countries are shown in Fig. 1.

The main symptoms of COVID-19 are a low fever, a new and ongoing cough, a loss or change to taste and smell. In UK, the vaccines approved were developed by Pfizer/BioNTech, Oxford/AstraZeneca, and Moderna. The joint committee on vaccination and immunization (JCVI) [2] determines the order in which people will be offered the vaccine. At April/2021, people aged 50 and over, people of clinically (extremely) vulnerable, people living or working in the care homes, and health care providers, people with a learning disability are being offered.

Two COVID-19 diagnosis methods are available. The first method is viral testing to test the existence of viral RNA fragments [3]. The shortcomings of swab test [4] are two folds: (i) the swab samples may be contaminated and (ii) it needs to wait from several hours to several days to get the results. The other method is chest imaging. There are two main different chest imaging available: chest computed tomography (CCT) and chest X-ray (CXR)

CCT is one of the best chest imaging techniques so far, because it provides the finest resolution and it is capable of recognizing extremely small nodules [5]. It provides high-quality volumetric 3D chest data. On the other hand, CXR performs poor on soft tissue contrast, and it only provides 2D image [6].

In this paper, we aim to fuse CCT and CXR images, and expects the fusion can improve the performance compared to using CCT or CXR individually. Besides, we create a novel multiple input deep convolutional attention network (MIDCAN) that can handle CCT and CXR images simultaneously, and present the diagnosis

[*] Corresponding authors.
E-mail addresses: yudongzhang@ieee.org (Y.-D. Zhang), 973306782@qq.com (X. Zhang), shuihuawang@ieee.org (S.-H. Wang).
[1] Yu-Dong Zhang & Zheng Zhang contributed equally to this paper.

https://doi.org/10.1016/j.patrec.2021.06.021
0167-8655/© 2021 Elsevier B.V. All rights reserved.

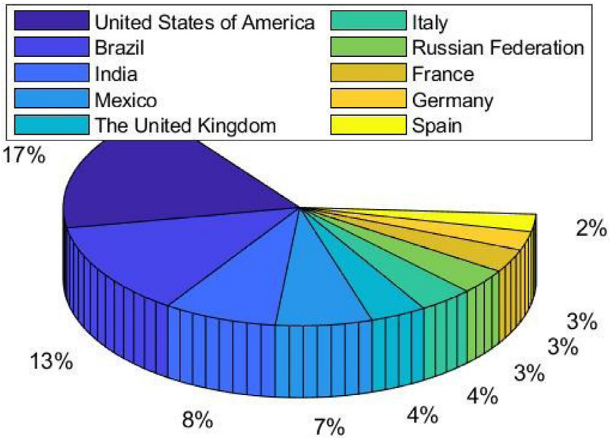

Fig. 1. Top 10 countries in terms of cumulative deaths (13/May/2021).

output. The contributions of this study are itemized briefly as following five points:

- Attention mechanism, convolutional block attention module, is included in the proposed MIDCAN model to improve the performance;
- The proposed MIDCAN model can handle CCT and CXR images simultaneously;
- Multiple-way data augmentation is employed to overcome overfitting problem;
- This proposed MIDCAN model gives more accurate performances than individual modality-based approaches;
- The proposed MIDCAN model is superior to state-of-the-art COVID-19 diagnosis approaches.

2. Literature survey

From previous year, AI field has investigated ongoing researches on automatic COVID-19 diagnosis, which can save the workloads of manual labelling.

For the CCT image based COVID-19 diagnosis, Chen (2020) [7] employed gray-level occurrence matrix (GLCM) as feature extraction method. The authors then used support vector machine (SVM) as the classifier. Yao (2020) [8] combined wavelet entropy (WE) and biogeography-based optimization (BBO). Wu (2020) [9] presented a novel method—wavelet Renyi entropy (WRE) to help diagnose COVID-19. El-kenawy, Ibrahim (2020) [10] proposed a feature selection voting classifier (FSVC) approach for COVID-19 classification. Satapathy (2021) [11] combined DenseNet with optimization of transfer learning setting (OTLS). Saood and Hatem (2021) [12] explored two structurally-different deep learning (DL) methods—U-Net and SegNet—for COVID-19 CT image segmentation.

On the other side, there are several successful AI models for CXR image based COVID-19 diagnosis. For example, Ismael and Sengur (2020) [13] presented a multi-resolution analysis (MRA) approach. Loey, Smarandache (2020) [14] combined generative adversarial network (GAN) with GoogleNet. Their method is abbreviated as GG. Togacar, Ergen (2020) [15] employed social mimic optimization (SMO) for feature selection and combination. Das, Ghosh (2021) [16] used weighted average ensembling technique with convolutional neural network (CNN) for automatic COVID-19 detection.

The main shortcomings of above approaches are three points: (i) They only consider individual modality, either CCT or CXR. (ii) Their AI models are either traditional feature extraction plus classifier model, or modern deep neural network models. Nevertheless, their models lack attention mechanism. (iii) Efficient measures to resist overfitting are missing.

Algorithm 1 Data harmonization.

```
Input    CCT image $A_0(n)$ and CXR image $B_0(n)$ of subject $n$.
Step 1   For CCT image $A_0(n)$
         64 central slices are reserved, and top/bottom slices are removed
Step 2   For CXR image $B_0(n)$
         Central rectangle region is reserved, and outskirt pixels are
         removed.
Step 3   CCT images are resized to 1024 × 1024, and CXR image is
         resized to 2048 × 2048.
Output   CCT image $A_1(n)$ and CXR image $B_1(n)$.
         $size[A_1(n)] = 1024 \times 1024 \times 64$.
         $size[B_1(n)] = 2048 \times 2048$.
```

To solve or alleviate above three shortcomings, we proposed the multiple input deep convolutional attention network. The dataset and details of our method will be discussed in Sections 3 and 4, respectively.

3. Dataset

3.1. Data harmonization

This retrospective study was granted to exempt ethical approval. 42 COVID-19 patients and 44 healthy controls (HCs) were recruited. All the data were collected from local hospitals. Each subject n takes a CCT scan a CXR scan, and thus generate a CCT image $A_0(n)$ and CXR image $B_0(n)$. Due to different chest sizes of different people and the different sources of scanning machines, the height of image $A_0(n)$ and the size of $B_0(n)$ vary.

To make a homogeneous dataset, data harmonization [17] is used. The central 64 slices of CCT image and the central rectangle region of CXR image are reserved. The height and width of CCT slices are resized to 1024 × 1024, and the CXR image is resized to 2048 × 2048. They are named $A_1(n)$ and $B_1(n)$. We choose 64 and 2048 because we find this can keep the lung part of images while get rid of unrelated body tissues. The details are displayed in Algorithm 1.

3.2. Data Preprocessing

Second, data preprocessing (See Fig. 2) is used since both CCT and CXR image contain redundant/unrelated spatial information and their sizes are still too large. First, all the CCT and CXR images are grayscaled. Second, histogram stretch is carried to enhance the image contrast, where (v_{min}, v_{max}) stand for the minimum and maximum grayscale values of our images. Third, the margins at four directions are cropped (e.g., the text in the right side and the check-up bed in bottom side of CCT images, the neck part in the top side of CXR images, the background regions at four directions, etc.). Finally, CCT images are resized to $H^{CCT} \times W^{CCT} \times C^{CCT}$ and CXR images are resized to $H^{CXR} \times W^{CXR} \times 1$.

Fig. 3 gives the examples of preprocessed images of a COVID-19 patient. Fig. 3(a) displays one slice out of 16 CCT slices, and Fig. 3(b) displays the CXR image.

4. Methodology

4.1. Convolutional block attention module

Table 1 gives the abbreviation list. DL has gained many successes in prediction/classification quests. Among all the DL structures, convolutional neural network (CNN) [18, 19] is particularly suitable for analyzing 2D/3D images. To help boost the performance of CNN, researches are proposed to modify CNN structures in terms of either depth, or cardinality, or width. Newly, scholars have studied on attention mechanism, and attempted to integrate attention to DL structures. For example, Hu, Shen (2020)

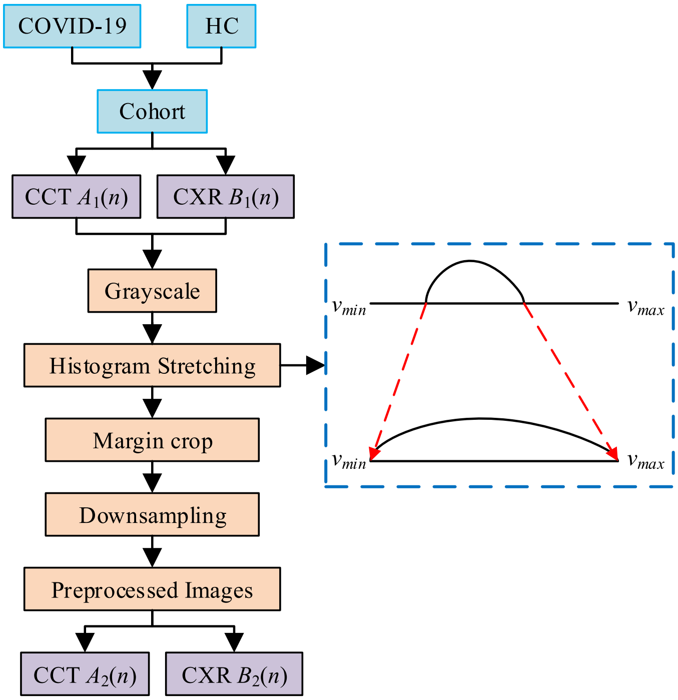

Fig. 2. Flowchart of preprocessing.

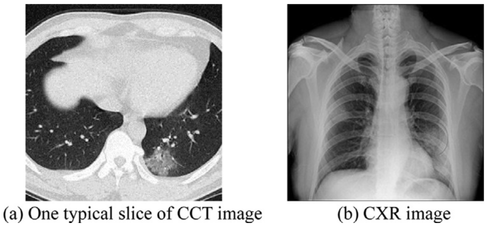
(a) One typical slice of CCT image

(b) CXR image

Fig. 3. Pre-processed images of one COVID-19 patient.

[20] proposed squeeze-and-excitation (SE) network. Woo, Park (2018) [21] presented a new convolutional block attention module (CBAM), that improves the traditional convolutional block (CB) by integrating attention mechanism. This study we choose CBAM because CBAM can provider both spatial attention and channel attention, compared to SE.

Take a 2D-image input as an example, Fig. 4(a) displays the structure of a traditional CB. The output of previous block was sent to m-repetitions of convolution layer, batch normalization (BN), and rectified linear unit (ReLU) layer. Finally, the m-repetitions is followed by a pooling layer. The output is named activation map (AM), symbolized as $\mathbf{G}\in\mathbb{R}^{C\times H\times W}$, where (C, H, W) stands for the sizes of channel, height, and width, respectively.

In contrast to Fig. 4(a), Fig. 4(b) adds the structure of CBAM, by which two modules: channel attention module (CAM) and spatial attention module (SAM) are added to refine the activation map $\mathbf{G}$. Suppose the CBAM applies a 1D CAM $\mathbf{N_{CAM}}\in\mathbb{R}^{C\times\ 1\ \times\ 1}$ and a 2D SAM $\mathbf{N_{SAM}}\in\mathbb{R}^{1\ \times H\times W}$ in sequence to the input $\mathbf{G}$. Hence, the channel-refined activation map can be obtained as:

$$\mathbf{H}=\mathbf{N_{CAM}}(\mathbf{D})\otimes\mathbf{G} \tag{1}$$

And the final refined AM

$$\mathbf{I}=\mathbf{N_{SAM}}(\mathbf{E})\otimes\mathbf{H} \tag{2}$$

where ⊗ means the element-wise multiplication. $\mathbf{I}$ is the refined AM, which replaces the $\mathbf{G}$ of traditional CB output, and it will be sent to the next block.

Table 1
Abbreviation list.

Meanings	Abbreviations
AM	activation map
AI	artificial intelligence
AP	average pooling
BN	batch normalization
CAM	channel attention module
CCT	chest computed tomography
CXR	chest X-ray
CB	convolutional block
CBAM	convolutional block attention module
CNN	convolutional neural network
DA	data augmentation
DL	deep learning
FMI	Fowlkes–Mallows index
MCC	Matthews correlation coefficient
MP	max pooling
MSD	mean and standard deviation
ReLU	rectified linear unit
SAPN	salt-and-pepper noise
SAM	spatial attention module
SN	speckle noise
SE	squeeze-and-excitation

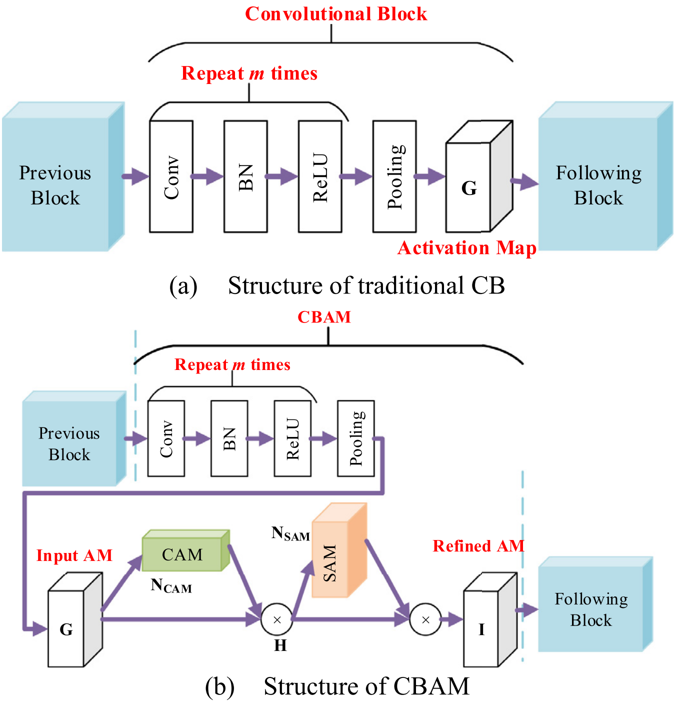

Fig. 4. Structural comparison.

Note if the above two operands are not with the same dimension, the values are reproduced so that (i) the spatial attentional values are copied along the channel dimension, and (ii) the channel attention values are copied along the spatial dimension.

4.2. Channel Attention Module

CAM is firstly defined. Both max pooling (MP) z_{mp} and average pooling (AP) z_{mp} are employed, making two features $\mathbf{J_{ap}}$ and $\mathbf{J_{mp}}$ as shown in Fig. 5(a).

$$\begin{cases}\mathbf{J_{ap}}=z_{ap}(\mathbf{G})\\ \mathbf{J_{mp}}=z_{mp}(\mathbf{G})\end{cases} \tag{3}$$

Both $\mathbf{J_{ap}}$ and $\mathbf{J_{mp}}$ are thenceforth sent to a shared multi-layer perceptron (MLP) to make the output AMs, that are then merged

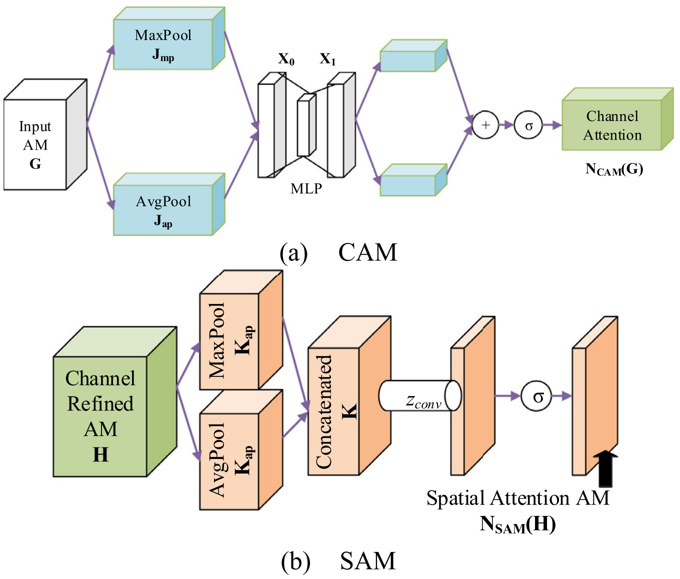

Fig. 5. Flowchart of two modules.

via element-wise summation $\oplus$. The merged sum $z_{mlp}[\mathbf{J_{ap}}] \oplus z_{mlp}[\mathbf{J_{mp}}]$ is lastly forwarded to σ. That is,

$$\mathbf{N_{CAM}}(\mathbf{G}) = \sigma\left\{z_{mlp}[\mathbf{J_{ap}}] \oplus z_{mlp}[\mathbf{J_{mp}}]\right\} \tag{4}$$

where σ is sigmoid function.

To decrease the parameter space, the hidden size of MLP is fixed to $\mathbb{R}^{C/r\times\ 1\ \times\ 1}$, where r stands for the reduction ratio. Assume $\mathbf{X_0} \in \mathbb{R}^{C/r\times C}$ and $\mathbf{X_1} \in \mathbb{R}^{C\times C/r}$ mean the MLP weights (See Fig. 5a), respectively, equation (4) can be rewritten as:

$$\mathbf{N_{CAM}}(\mathbf{G}) = \sigma\{\mathbf{X_1}[\mathbf{X_0}(\mathbf{J_{ap}})] \oplus \mathbf{X_1}[\mathbf{X_0}(\mathbf{J_{mp}})]\} \tag{5}$$

Note $\mathbf{X_0}$ and $\mathbf{X_1}$ are shared by both $\mathbf{J_{ap}}$ and $\mathbf{J_{mp}}$. Fig. 5(a) displays the diagram of CAM.

4.3. Spatial Attention Module

Next, SAM is defined in Fig. 5(b). The spatial attention module $\mathbf{N_{SAM}}$ is a complementary procedure to the previous CAM $\mathbf{N_{CAM}}$. The average pooling z_{ap} and max pooling z_{mp} are harnessed again to the channel-refined activation map $\mathbf{H}$,

$$\begin{cases} \mathbf{K_{ap}} = z_{ap}(\mathbf{H}) \\ \mathbf{K_{mp}} = z_{mp}(\mathbf{H}) \end{cases} \tag{6}$$

Both $\mathbf{K_{ap}}$ and $\mathbf{K_{mp}}$ are two dimensional AMs: $\mathbf{K_{ap}} \in \mathbb{R}^{1\ \times H\times W} \wedge \mathbf{K_{mp}} \in \mathbb{R}^{1\ \times H\times W}$. They are concatenated via concatenation function z_{con} together along the channel dimension as

$$\mathbf{K} = z_{con}(\mathbf{K_{ap}}, \mathbf{K_{mp}}) \tag{7}$$

Afterwards, the concatenated AM is passed into a standard convolution z_{conv} with the size of 7 × 7, followed by sigmoid function σ. Overall, we attain:

$$\mathbf{N_{SAM}}(\mathbf{H}) = \sigma\{z_{conv}[\mathbf{K}]\} \tag{8}$$

The $\mathbf{N_{SAM}}(\mathbf{H})$ is then element-wisely multiplied by $\mathbf{H}$ to get the final refined AE $\mathbf{I}$. See Equation (2). The diagram of SAM is portrayed in Fig. 5(b).

4.4. Single Input and Multiple Input Deep Convolutional Attention Networks

In this study, we proposed a novel multiple-input deep convolutional attention network (MIDCAN) based on the ideas of CBAM and multiple-input. The structure of this proposed MIDCAN is determined by trial-and-error method. The variable m in each block varies, and we found the best values are chosen in the range from $[1, 3]$. We tested values larger than 3, which increase the computation burden, but the performances do not increase.

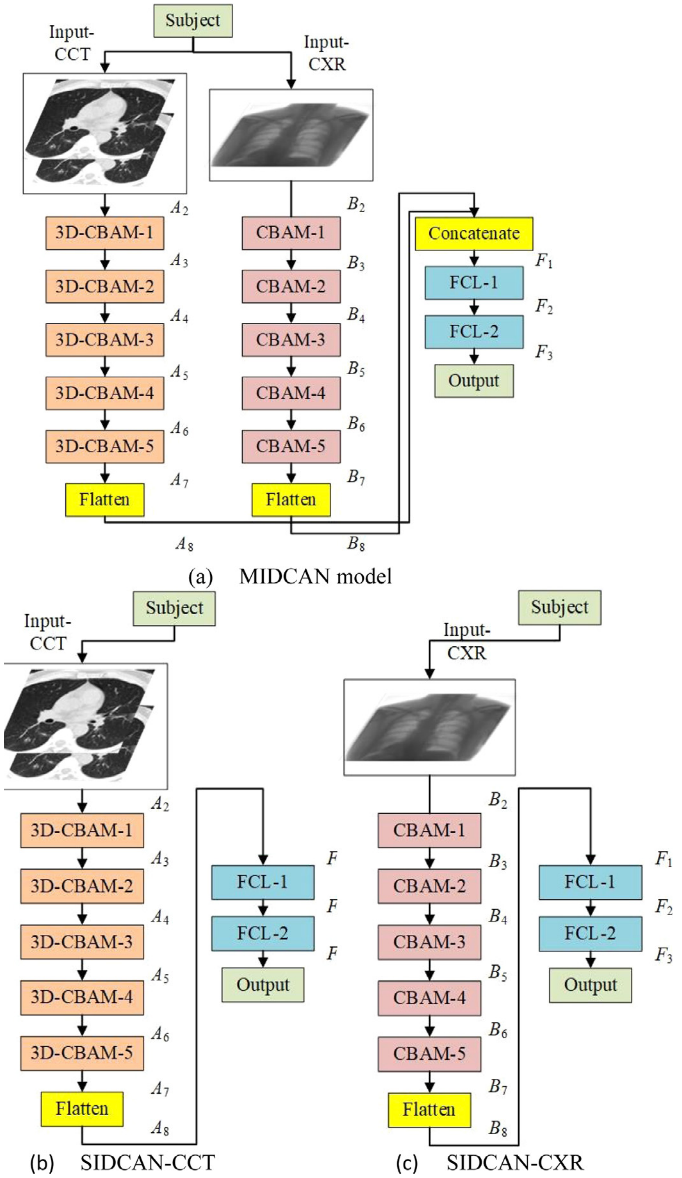

Fig. 6. Variables and sizes of AMs of three proposed models.

The structure of proposed shown below in Fig. 6(a), which is composed of two inputs. The left input is “Input-CCT” where CCT images are passed into the network. The right input is “Input-CXR” where CXR images are passed into the network. Suppose N_C^{CCT} and N_C^{CXR} stand for the number of CBAM blocks individually. We set $N_C^{CCT} = N_C^{CXR} = 5$ in this study by trial-and-error.

For the left branch, the CCT input A_2 goes through N_C^{CCT} 3D-CBAMs and generates the output AM A_7, which is then flattened into A_8. Similarly, the CXR input at right branch B_2 goes through N_C^{CXR} 2D-CBAMs, generates the output AM B_7, which is flattened into B_8. The deep CCT features and deep CXR features are then concatenated via concatenation function z_{con} as

$$\text{MIDCAN}: F_1 = z_{con}(A_8, B_8) \tag{9}$$

Here note than in our experiments, we use ablation studies, where we set two models: single-input deep convolutional atten-

Table 2
Details of proposed MIDCAN model.

Name	Kernel Parameter	Variable and size
Input-CCT		$size(A_2) = 256 \times 256 \times 16$
3D-CBAM-1	[3 × 3 × 3, 16]x3, [/2/2/2]	$size(A_3) = 128 \times 128 \times 8 \times 16$
3D-CBAM-2	[3 × 3 × 3, 32]x2, [/2/2/1]	$size(A_4) = 64 \times 64 \times 8 \times 32$
3D-CBAM-3	[3 × 3 × 3, 32]x2, [/2/2/2]	$size(A_5) = 32 \times 32 \times 4 \times 32$
3D-CBAM-4	[3 × 3 × 3, 64]x2, [/2/2/1]	$size(A_6) = 16 \times 16 \times 4 \times 64$
3D-CBAM-5	[3 × 3 × 3, 64]x2, [/2/2/2]	$size(A_7) = 8 \times 8 \times 2 \times 64$
Flatten		$size(A_8) = 8192$
Input-CXR		$size(B_2) = 256 \times 256$
CBAM-1	[3 × 3, 16]x3, [/2/2]	$size(B_3) = 128 \times 128 \times 16$
CBAM-2	[3 × 3, 32]x2, [/2/2]	$size(B_4) = 64 \times 64 \times 32$
CBAM-3	[3 × 3, 64]x2, [/2/2]	$size(B_5) = 32 \times 32 \times 64$
CBAM-4	[3 × 3, 64]x2, [/2/2]	$size(B_6) = 16 \times 16 \times 64$
CBAM-5	[3 × 3, 128]x2, [/2/2]	$size(B_7) = 8 \times 8 \times 128$
Flatten		$size(B_8) = 8192$
Concatenate		$size(F_1) = 16,384$
FCL-1	500 × 16384, 500 × 1	$size(F_2) = 500$
FCL-2	2 × 500, 2 × 1	$size(F_3) = 2$
Softmax		

tion network (SIDCAN) models, which remove the left and right branches, respectively. The first SIDCAN model, shown in Fig. 6(b), will only use CCT features, i.e.,

$$\text{SIDCAN} - \text{CCT} : F_1 = A_8 \tag{10}$$

This model is given a short name as SIDCAN-CCT.

The second SIDCAN model will only use CXR features, i.e.,

$$\text{SIDCAN} - \text{CXR} : F_1 = B_8 \tag{11}$$

This model is named as SIDCAN-CXR. Its flowchart is displayed in Fig. 6(c). Those two models will used as comparison method in our experiments.

The feature F_1 is then passed to two fully-connected layers [22]. The first FCL contains 500 neurons, and the last FCL contains N_C neurons, where N_C stands for the number of classes. In this study $N_C = 2$. Finally, a softmax layer [23] turns the F_3 to probability. The loss function of this MIDCAN is cross entropy [24] function.

Table 2 gives the details of proposed MIDCAN. For the kernel parameter in Table 2, [3 × 3 × 3, 16]x3, [/2/2/2] stands for 3 repetitions of 16 filters with each size of 3 × 3 × 3, following by a pooling with pooling factor of 2, 2, and 2 along three dimensions, respectively. In FCL stage, the kernel parameter gives the size of weight matrix and bias vector, respectively.

4.5. 18-way data augmentation

Data augmentation (DA) [25] is an important utensil over the training set to avoid overfitting of classifiers when applied to test set. Meanwhile, DA can overcome the small-size dataset problem. Recently, Wang (2021) [26] proposed a novel 14-way data augmentation (DA), which used seven different DA techniques to the preprocessed training image $v(k)$ and its horizontal mirrored image $v^H(k)$, respectively. Cheng (2021) [27] presented a 16-way DA, and used PatchShuffle technique to avoid overfitting.

This study enhances the 14-way DA method [26] to 18-way DA, by adding two new DA methods: salt-and-pepper noise (SAPN) and speckle noise (SN) on both $v(k)$ and $v^H(k)$. Use $v(k)$ as an example, the SAPN altered image is symbolized as $v^{SAPN}(k)$ with its values are set as

$$\begin{cases} \mathbf{R}\left(v^{SAPN} = v\right) = 1 - \gamma_d^{sa}, \\ \mathbf{R}\left(v^{SAPN} = v_{min}\right) = \frac{\gamma_d^{sa}}{2}, \\ \mathbf{R}\left(v^{SAPN} = v_{max}\right) = \frac{\gamma_d^{sa}}{2}, \end{cases} \tag{12}$$

where γ_d^{sa} stands for noise density, and $\mathbf{R}$ the probability function. $v_{\min}$ and $v_{\max}$ correspond to black and white colors, respectively.

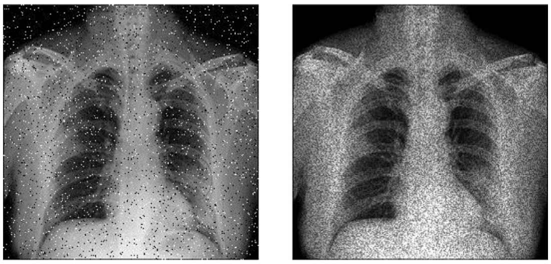
(a) SAPN altered (b) SN altered

Fig. 7. Examples of newly proposed DA methods.

On the other side, the SN altered image is defined as

$$v^{SN}(k) = v(k) + \mathbb{U} \times v(k), \tag{13}$$

where $\mathbb{U}$ is a uniformly distributed random noise, of which the mean and variance are symbolized as U_m^{sn} and U_v^{sn}, respectively. Take Fig. 3(b) as the example, Fig. 7(a-b) display the SAPN and SN altered images, respectively. Due to the page limit, the results of other DA are not shown in this paper.

Let M_a stands for the number of DA techniques to the preprocessed image $v(k)$, and M_b stands for the number of new generated images for each DA. This proposed $(2 \times M_a)$-way DA algorithm is a four-step algorithm depicted below:

First, M_a geometric/photometric/noise-injection DA transforms are utilized on preprocessed train image $v(k)$,. We use $w_{(m)}^{DA}, m = 1, \ldots, M_a$ to denote each DA operation. See each DA operations $w_{(m)}^{DA}$ yields M_b new images. Thus, for a given image $t(k)$, we yield M_a different data set $w_{(m)}^{DA}[v(k)], m = 1, \cdots, M_a$, and each dataset contains M_b new images.

Second, horizontally mirrored image is generated as

$$v^H(k) = z_M[v(k)], \tag{14}$$

where z_M means horizontal mirror function.

Third, all the M_a DA methods are carried out on the mirror image $v^H(k)$, and generate M_a different dataset $w_{(m)}^{DA}[v^H(k)], m = 1, \cdots, M_a$.

Four, the raw image $v(k)$, the horizontally mirrored image $v^H(k)$, all M_a-way results of preprocessed image $w_{(m)}^{DA}[v(k)], m = 1, \cdots, M_a$, and M_a-way DA results of horizontally mirrored image $w_{(m)}^{DA}[v^H(k)], m = 1, \cdots, M_a$, are fused together using concatenation function z_{CON}, as defined in Eq. (9).

The final combined dataset is defined as Λ

$$v(k) \mapsto \Lambda = z_{con}\left\{\begin{array}{cc} v(k) & v^H(k) \\ \underbrace{w_{(1)}^{DA}[v(k)]}_{M_b} & \underbrace{w_{(1)}^{DA}\left[v^H(k)\right]}_{M_b} \\ \cdots & \cdots \\ \underbrace{w_{(M_a)}^{DA}[v(k)]}_{M_b} & \underbrace{w_{(M_a)}^{DA}\left[v^H(k)\right]}_{M_b} \end{array}\right\} \tag{15}$$

Therefore, one image $v(k)$ will generate

$$|\Lambda| = 2 \times M_a \times M_b + 2 \tag{16}$$

images (including the original image $v(k)$). Note in our dataset, different M_b will be assigned to CCT training images and CXR images since CCT images are 3D and CXR images are 2D. That means for each DA, we have M_b^{CCT} new images for each CCT image and M_b^{CXR} new images for each CXR image.

4.6. Implementation and evaluation

K-fold cross validation is employed on both datasets. Suppose confusion matrix $\mathbf{J}$ over r-th $(1 \le r \le R)$ run and k-th $(1 \le k \le K)$

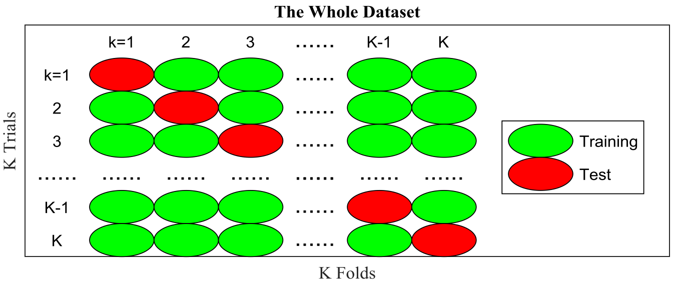

Fig. 8. Diagram of one run of K-fold cross validation.

fold is defined as

$$\mathbf{J}(r,k)=\begin{bmatrix} j_{11}(r,k) & j_{12}(r,k) \\ j_{21}(r,k) & j_{22}(r,k) \end{bmatrix} \tag{17}$$

where $(j_{11}, j_{12}, j_{21}, j_{22})$ stand for TP, FN, FP, and TN, respectively. P stands for positive class, i.e., COVID-19, and N means negative class, i.e., healthy control. k represents the index of trial/fold, and r stands for the index of run. At k-th trial, the k-th fold is used as test, and all the left folds are used as training,

Note that $\mathbf{J}(r,k)$ is calculated based on each test fold, and are then summarized across all K trials, as shown in Fig. 8. Afterwards, we get the confusion matrix at r-th run $\mathbf{J}(r)$ as

$$\mathbf{J}(r)=\sum_{k=1}^{K}\mathbf{J}(r,k) \tag{18}$$

Seven indicators $\vec{\tau}(r)$ are computed based on the confusion matrix over r-th run $\mathbf{J}(r)$.

$$\mathbf{J}(r)\mapsto\vec{\eta}(r)=[\eta_1(r),\eta_2(r),\cdots,\eta_7(r)], \tag{19}$$

where first four indicators are: η_1 sensitivity, η_2 specificity, η_3 precision, and η_4 accuracy. Those four indicators are commonly used. Their definitions can be found easily. η_5 is F1 score.

$$\eta_5(r)=\frac{2\ \times j_{11}(r)}{2\ \times j_{11}(r)+j_{12}(r)+j_{21}(r)} \tag{20}$$

η_6 is Matthews correlation coefficient (MCC)

$$\eta_6(r)=\frac{j_{11}(r)\times j_{22}(r)-j_{21}(r)\times j_{12}(r)}{\sqrt{[j_{11}(r)+j_{21}(r)]\times[j_{11}(r)+j_{12}(r)]\times[j_{22}(r)+j_{21}(r)]\times[j_{22}(r)+j_{12}(r)]}} \tag{21}$$

and η_7 is the Fowlkes–Mallows index (FMI).

$$\eta_7(r)=\sqrt{\frac{j_{11}(r)}{j_{11}(r)+l_{21}(r)}\times\frac{j_{11}(r)}{j_{11}(r)+j_{21}(r)}} \tag{22}$$

There are two indicators η_4 and η_6 using all the four basic measures $(j_{11}, j_{12}, j_{21}, j_{22})$. Considering the range of η_4 is $0\le\eta_4\le1$, and the range of η_6 is $-1\le\eta_6\le+1$, we finally choose η_6 as the most important indicator. Besides, Chicco, Totsch (2021) [28] stated that MCC is more reliable than many other indicators.

Above procedure is one run of K-fold cross validation. We run the K-fold cross validation R runs. The mean and standard deviation (MSD) of all seven indicators $\eta_m(m=1,\dots,7)$ are calculated over all R runs.

$$\begin{cases}\mu(\eta_m)=\frac{1}{R}\times\sum\limits_{r=1}^{R}\eta_m(r)\\ \sigma(\eta_m)=\sqrt{\frac{1}{R-1}\times\sum\limits_{r=1}^{R}|\eta_m(r)-\mu(\eta_m)|^2}\end{cases} \tag{23}$$

where μ stands for the mean value, and σ stands for the standard deviation. The MSDs are reported in the format of $\eta=\mu(\eta)\pm\sigma(\eta)$.

Table 3
Parameter setting.

Parameter	Value
$(\upsilon_{min},\upsilon_{,max})$	(0, 255)
$H^{CCT}\times W^{CCT}\times C^{CCT}$	256 × 256 × 16
$H^{CXR}\times W^{CXR}$	256 × 256
N_C^{CCT}	5
N_C^{CXR}	5
γ_d^{sa}	0.05
U_m^{sn}	0
U_v^{sn}	0.05
M_a	9
M_b^{CXR}	30
M_b^{CCT}	90
K	10
R	10

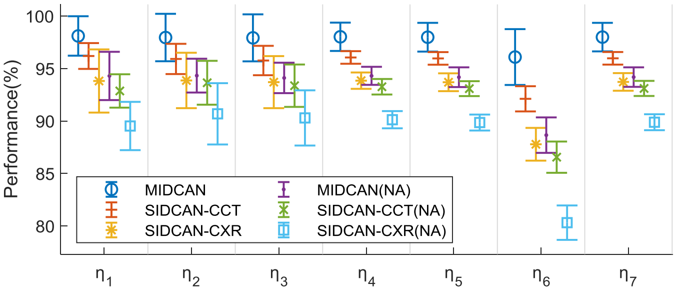

Fig. 9. Error bar comparison of six different settings.

5. Experiments, results, and discussions

5.1. Parameter setting

Table 3 itemizes the parameter setting. Here the minimum value and maximum value of our images are set to 0 and 255, respectively. The size of preprocessed CCT images and CXR images are set to 256 × 256 × 16 and 256 × 256, respectively. The number of CBAM blocks for CCT and CXR branches are set to 5. The noise density of SAPN is set to 0.05. The mean and variance of uniform distributed noise in SN are set to 0 and 0.05, respectively. Nine different DA methods are used, so we have an 18-way DA if we consider both raw training image and its horizontal mirrored image. For each DA, 30 new images are generated for each CXR image, and 90 new images are generated for each CCT image. The number of K-fold is set to $K=10$. We run our model $R=10$ runs.

5.2. Statistics of proposed MIDCAN

We use two modalities, CCT and CXR, in this experiment. The structure of our model is shown in Fig. 6(a). The statistical results of proposed MIDCAN are shown in Table 4. As it shows, the sensitivity, specificity, precision and accuracy are 98.10±1.88, 97.95±2.26, 97.92±2.24, and 98.02±1.35, respectively. Moreover, the F1 score is 97.98±1.37, the MCC is 96.09±2.66, and FMI is 97.99±1.36.

5.3. Effect of multimodality and attention mechanism

We compare multiple-modality against single-modality. Two models, viz., SIDCAN-CCT and SIDCAN-CXR, shown in Fig. 6(b-c)

Table 4
Statistical results of proposed MIDCAN model.

Run	η_1	η_2	η_3	η_4	η_5	η_6	η_7
1	97.62	100.00	100.00	98.84	98.80	97.70	98.80
2	97.62	97.73	97.62	97.67	97.62	95.35	97.62
3	100.00	100.00	100.00	100.00	100.00	100.00	100.00
4	100.00	97.73	97.67	98.84	98.82	97.70	98.83
5	95.24	97.73	97.56	96.51	96.39	93.04	96.39
6	100.00	93.18	93.33	96.51	96.55	93.26	96.61
7	100.00	100.00	100.00	100.00	100.00	100.00	100.00
8	97.62	95.45	95.35	96.51	96.47	93.05	96.48
9	95.24	100.00	100.00	97.67	97.56	95.44	97.59
10	97.62	97.73	97.62	97.67	97.62	95.35	97.62
MSD	98.10	97.95	97.92	98.02	97.98	96.09	97.99
	±1.88	±2.26	±2.24	±1.35	±1.37	±2.66	±1.36

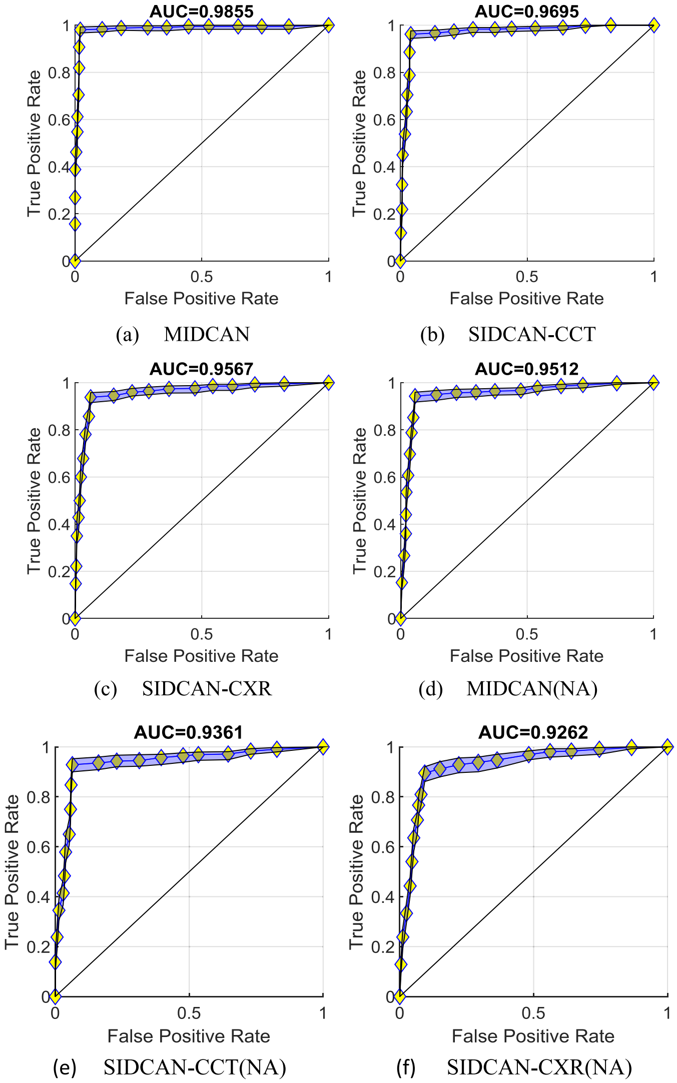

(a) MIDCAN

(b) SIDCAN-CCT

(c) SIDCAN-CXR

(d) MIDCAN(NA)

(e) SIDCAN-CCT(NA)

(f) SIDCAN-CXR(NA)

Fig. 10. ROC curves of six settings.

are used. Meanwhile, using attention and not using attention are compared.

The comparison results are shown in Table 5, where NA means no attention. Fig. 9 presents the error bar comparison of all the six setting. Comparing using attention against without using attention, we can observe the attention mechanism does help improve the classification performance, which is coherent with the conclusion of Ref. [21].

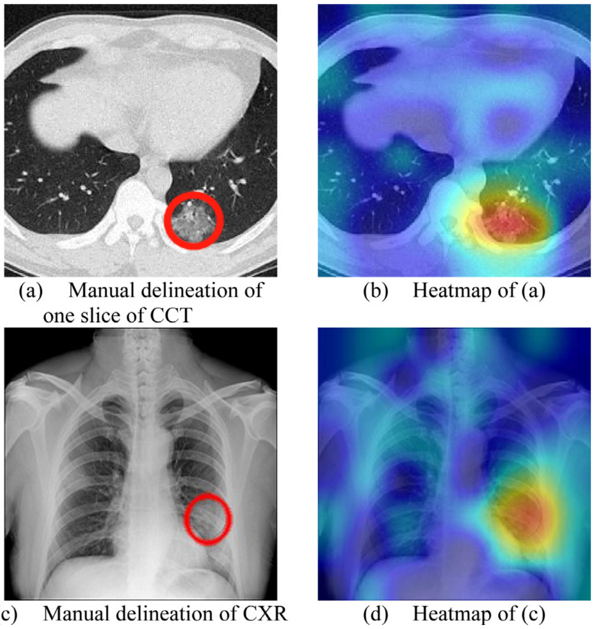

(a) Manual delineation of one slice of CCT

(b) Heatmap of (a)

(c) Manual delineation of CXR

(d) Heatmap of (c)

Fig. 11. Manual delineation and heatmap results of one patient.

Meanwhile, if we compare MIDCAN with two SIDCAN models, we can conclude that multimodality has the better performance than single modalities (both CT and CXR).

Fig. 10 displays the ROC curves of six settings. The blue patch corresponds to the lower bound and upper bound. For the first three models using attention, we can observe their AUCs are 0.9855, 0.9695, and 0.9567 for MIDCAN, SIDCAN-CCT, and SIDCAN-CXR, respectively. If removing the CBAM module, we can observe from the bottom part of Fig. 10, that the corresponding AUCs decrease to 0.9512, 0.9361, and 0.9262, respectively. In addition, multimodality is proven to give better performance than using single-modality.

5.4. Explainability of proposed model

Fig. 11 presents the manual delineation and heatmap results of Fig. 3. The heatmap images are generated via Grad-CAM method [29].

From Fig. 11, we can observe the proposed MIDCAN model is able to capture the lesions of both CCT image and CXR image accurately. This explainability via Grad-CAM can help the doctors, radiologists, and patients to better understand how our AI model works.

Table 5
Comparison of different settings.

Method	η_1	η_2	η_3	η_4	η_5	η_6	η_7
MIDCAN	98.10 ±1.88	97.95 ±2.26	97.92 ±2.24	98.02 ±1.35	97.98 ±1.37	96.09 ±2.66	97.99 ±1.36
SIDCAN -CCT	96.19 ±1.23	95.91 ±1.44	95.76 ±1.40	96.05 ±0.60	95.96 ±0.60	92.11 ±1.20	95.97 ±0.60
SIDCAN-CXR	93.81 ±3.01	93.86 ±2.64	93.70 ±2.48	93.84 ±0.78	93.69 ±0.85	87.78 ±1.56	93.72 ±0.84
MIDCAN (NA)	94.29 ±2.30	94.32 ±1.61	94.10 ±1.45	94.30 ±0.86	94.17 ±0.94	88.65 ±1.69	94.18 ±0.93
SIDCAN-CCT(NA)	92.86 ±1.59	93.64 ±2.09	93.36 ±2.02	93.26 ±0.74	93.08 ±0.71	86.55 ±1.49	93.10 ±0.72
SIDCAN-CXR(NA)	89.52 ±2.30	90.68 ±2.92	90.29 ±2.63	90.12 ±0.82	89.85 ±0.76	80.31 ±1.64	89.88 ±0.76

Table 6
Comparison with SOTA approaches (Unit: %).

Approach	η_1	η_2	η_3	η_4	η_5	η_6	η_7
GLCM [7]	71.90 ±4.02	78.18 ±3.89	76.04 ±2.41	75.12 ±0.98	73.80 ±1.49	50.35 ±1.91	73.89 ±1.39
WE-BBO [8]	74.05 ±4.82	74.77 ±3.93	73.83 ±1.84	74.42 ±0.78	73.81 ±1.65	48.98 ±1.65	73.88 ±1.67
WRE [9]	86.43 ±3.18	86.36 ±3.86	86.01 ±3.13	86.40 ±0.56	86.12 ±0.39	72.95 ±1.15	86.17 ±0.40
FSVC [10]	91.90 ±2.56	90.00 ±2.44	89.85 ±1.99	90.93 ±0.49	90.82 ±0.55	81.97 ±0.99	90.85 ±0.56
OTLS [11]	95.95 ±2.26	96.59 ±1.61	96.45 ±1.56	96.28 ±1.07	96.17 ±1.13	92.60 ±2.09	96.19 ±1.12
MRA [13]	86.43 ±3.90	90.45 ±2.79	89.71 ±2.63	88.49 ±2.08	87.98 ±2.27	77.09 ±4.17	88.02 ±2.26
GG [14]	93.33 ±2.70	90.00 ±4.44	90.13 ±3.81	91.63 ±1.53	91.61 ±1.35	83.49 ±2.84	91.67 ±1.30
SMO [15]	93.10 ±2.37	95.23 ±2.50	94.99 ±2.45	94.19 ±1.10	93.99 ±1.13	88.45 ±2.16	94.02 ±1.11
MIDCAN (Ours)	98.10 ±1.88	97.95 ±2.26	97.92 ±2.24	98.02 ±1.35	97.98 ±1.37	96.09 ±2.66	97.99 ±1.36

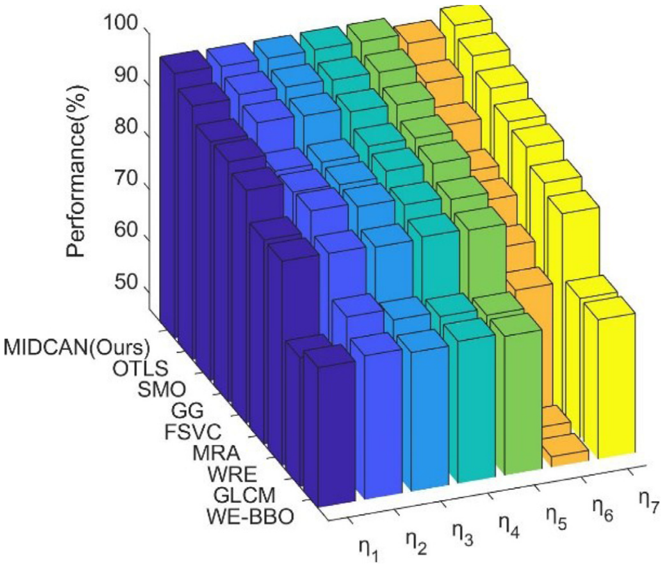

Fig. 12. 3D bar plot of approach comparison.

5.5. Comparison to State-of-the-art approaches

We compare the proposed method “MIDCAN” with 8 state-of-the-art methods: GLCM [7], WE-BBO [8], WRE [9], FSVC [10], OTLS [11], MRA [13], GG [14], SMO [15]. Those methods were carried out on single modality dataset depending on their original paper reported (either CCT or CXR), so we test those methods in the corresponding SIDCAN models and single-modality dataset.

All the methods were evaluated via 10 runs of 10-fold cross validation. The MSD results $\vec{\eta}$ of all approaches on ten runs of 10-fold cross validation are pictured in Fig. 12, which sorts all the methods in terms of η_6, and itemized in Table 6.

From Table 6, we can observe that this proposed MIDCAN outperforms all the other 8 comparison baseline methods in terms of all indicators.

The reason why our MIDCAN method is the best lie in following three facts: (i) we propose to use multiple modality instead of traditional single modality; (ii) CBAM is used in our network that attention mechanism can help our AI model focuses on the lesion region; (iii) multiple-way data augmentation is employed to overcome overfitting.

6. Conclusion

This paper proposed a novel multiple input deep convolutional attention network (MIDCAN) model for diagnosis of COVID-19. The results show our method achieves a sensitivity of 98.10±1.88%, a specificity of 97.95±2.26%, and an accuracy of 98.02±1.35%.

In the future researches, we shall carry out several attempts: (i) expand our dataset; (ii) include other advanced network strategies, such as graph neural network; (iii) collect IoT signals of subjects.

Declaration of Competing Interest

The authors declare that they have no known competing financial interests or personal relationships that could have appeared to influence the work reported in this paper.

Acknowledgment

This paper is partially supported by Medical Research Council Confidence in Concept Award, UK (MC_PC_17171); Hope Foundation for Cancer Research, UK (RM60G0680); British Heart Foundation Accelerator Award, UK; Sino-UK Industrial Fund, UK (RP202G0289); Global Challenges Research Fund (GCRF), UK (P202PF11); Royal Society International Exchanges Cost Share Award, UK (RP202G0230).

References

[1] K. Turgutalp, et al., Determinants of mortality in a large group of hemodialysis patients hospitalized for COVID-19, BMC Nephrol. 22 (1) (2021) 10 Article ID. 29.
[2] A.J. Hall, The United Kingdom joint committee on vaccination and immunisation, Vaccine 28 (2010) A54–A57.
[3] D. Sakanashi, et al., Comparative evaluation of nasopharyngeal swab and saliva specimens for the molecular detection of SARS-CoV-2 RNA in Japanese patients with COVID-19, J. Infect. Chemother. 27 (1) (2021) 126–129.
[4] C. Giannitto, et al., Chest CT in patients with a moderate or high pretest probability of COVID-19 and negative swab, Radiol. Med. (Torino) 125 (12) (2020) 1260–1270.
[5] R.L. Draelos, et al., Machine-learning-based multiple abnormality prediction with large-scale chest computed tomography volumes, Med. Image Anal. 67 (2021) 12 Article ID. 101857.
[6] A. Braga, et al., When less is more: regarding the use of chest X-ray instead of computed tomography in screening for pulmonary metastasis in postmolar gestational trophoblastic neoplasia, Br. J. Cancer (2021), doi:10.1038/s41416-020-01209-5.
[7] Y. Chen, Covid-19 classification based on gray-level co-occurrence matrix and support vector machine, in: in COVID-19: Prediction, Decision-Making, and its Impacts, Springer Singapore, Singapore, 2020, pp. 47–55. K.C. Santosh and A. Joshi, Editors.
[8] X. Yao, COVID-19 detection via wavelet entropy and biogeography-based optimization, in: in COVID-19: Prediction, Decision-Making, and its Impacts, Springer, 2020, pp. 69–76. K.C. Santosh and A. Joshi, Editors.
[9] X. Wu, Diagnosis of COVID-19 by wavelet Renyi entropy and three-segment biogeography-based optimization, Int. J. Comput. Intell. Syst. 13 (1) (2020) 1332–1344.
[10] E.S.M. El-kenawy, et al., Novel feature selection and voting classifier algorithms for COVID-19 classification in CT images, IEEE Access 8 (2020) 179317–179335.
[11] S.C. Satapathy, Covid-19 diagnosis via DenseNet and optimization of transfer learning setting, Cognitive Comput. (2021), doi:10.1007/s12559-020-09776-8.
[12] A. Saood, et al., COVID-19 lung CT image segmentation using deep learning methods: U-Net versus SegNet, BMC Med. Imaging 21 (1) (2021) 10 Article ID. 19.
[13] A.M. Ismael, et al., The investigation of multiresolution approaches for chest X-ray image based COVID-19 detection, Health Inf. Sci. Syst. 8 (1) (2020) Article ID. 29.
[14] M. Loey, et al., Within the lack of chest COVID-19 X-ray dataset: a novel detection model based on GAN and deep transfer learning, Symmetry-Basel 12 (4) (2020) Article ID. 651.
[15] M. Togacar, et al., COVID-19 detection using deep learning models to exploit Social Mimic Optimization and structured chest X-ray images using fuzzy color and stacking approaches, Comput. Biol. Med. 121 (2020) 12 Article ID. 103805.
[16] A.K. Das, et al., Automatic COVID-19 detection from X-ray images using ensemble learning with convolutional neural network, Pattern Anal. Appl. (2021) 14, doi:10.1007/s10044-021-00970-4.
[17] R. Susukida, et al., Data management in substance use disorder treatment research: Implications from data harmonization of National Institute on Drug Abuse-funded randomized controlled trials, Clin. Trials (2021) 11, doi:10.1177/1740774520972687.
[18] K. Kumari, et al., Multi-modal aggression identification using convolutional neural network and binary particle swarm optimization, Future Generat. Comput. Syst. Int. J. Escience 118 (2021) 187–197.
[19] A.M. Hamer, et al., Replacing human interpretation of agricultural land in Afghanistan with a deep convolutional neural network, Int. J. Remote Sens. 42 (8) (2021) 3017–3038.
[20] J. Hu, et al., Squeeze-and-excitation networks, IEEE Trans. Pattern Anal. Mach. Intell. 42 (8) (2020) 2011–2023.
[21] S. Woo, et al., CBAM: Convolutional block attention module, in: Proceedings of the European conference on computer vision (ECCV), Munich, Germany, Springer, 2018, pp. 3–19.
[22] H. Sindi, et al., Random fully connected layered 1D CNN for solving the Z-bus loss allocation problem, Measurement 171 (2021) 8 Article ID. 108794.
[23] A. Kumar, et al., Topic-document inference with the gumbel-softmax distribution, IEEE Access 9 (2021) 1313–1320.
[24] P.D. Sathya, et al., Color image segmentation using Kapur, Otsu and minimum cross entropy functions based on exchange market algorithm, Expert Syst. Appl. 172 (2021) 30 Article ID. 114636.
[25] S. Kim, et al., Synthesis of brain tumor multicontrast MR images for improved data augmentation, Med. Phys. (2021) 14, doi:10.1002/mp.14701.
[26] S.-H. Wang, Covid-19 classification by FGCNet with deep feature fusion from graph convolutional network and convolutional neural network, Inf. Fusion 67 (2021) 208–229.
[27] X. Cheng, PSSPNN: PatchShuffle stochastic pooling neural network for an explainable diagnosis of COVID-19 with multiple-way data augmentation, Comput. Math. Methods Med. 2021 (2021) Article ID. 6633755.
[28] D. Chicco, et al., The Matthews correlation coefficient (MCC) is more reliable than balanced accuracy, bookmaker informedness, and markedness in two–class confusion matrix evaluation, Biodata Mining 14 (1) (2021) 22 Article ID. 13.
[29] R.R. Selvaraju, et al., Grad-CAM: visual explanations from deep networks via gradient-based localization, Int. J. Comput. Vision 128 (2) (2020) 336–359.